IEEE Access
Multidisciplinary | Rapid Review | Open Access Journal

Received October 1, 2021, accepted October 22, 2021, date of publication October 27, 2021, date of current version November 3, 2021.

Digital Object Identifier 10.1109/ACCESS.2021.3123358

Optimal Modulation Technique for Underwater Visible Light Communication Using Rolling-Shutter Sensor

RITSUKI HAMAGAMI[1], (Graduate Student Member, IEEE), TADASHI EBIHARA[2], (Member, IEEE), NAOTO WAKATSUKI[2], AND KOICHI MIZUTANI[2]

[1]Intelligent and Mechanical Interaction Systems, University of Tsukuba, Tsukuba 305-8577, Japan
[2]Faculty of Engineering, Information and Systems, University of Tsukuba, Tsukuba 305-8577, Japan

Corresponding author: Tadashi Ebihara (ebihara@iit.tsukuba.ac.jp)

This work was supported by the Japan Society for the Promotion of Science (JSPS) KAKENHI under Grant JP18K19774.

ABSTRACT The visible light communication (VLC) technique using a rolling-shutter sensor-based commercial camera has an advantage in that the LED and camera mounted on an underwater device (*e.g.*, drone, sensor) can be effectively used as a transmitter (Tx) and a receiver (Rx), respectively, under water. On the other hand, a suitable modulation technique has not been well considered to realize a VLC system using a rolling-shutter sensor in an underwater channel that includes high ambient light conditions. In this paper, we design VLC systems using phase-shift keying (PSK), non-return-to-zero on-off keying (NRZ-OOK), and orthogonal frequency division multiplexing (OFDM), and evaluate them through simulations and experiments. The results suggested that the VLC system using PSK or OFDM is more resilient than that using NRZ-OOK in an underwater channel with low-frequency ambient light, and that a VLC system using PSK or NRZ-OOK is more tolerant than that using OFDM in environments with high ambient light, resulting in pixel saturation. In conclusion, the present study has demonstrated that PSK is the most suitable modulation technique for a VLC system using a rolling-shutter sensor in an underwater channel that includes high ambient light conditions.

INDEX TERMS Visible light communication, rolling-shutter sensor, phase-shift keying, CMOS image sensor, underwater wireless communication.

I. INTRODUCTION

Underwater wireless communication is an enabling technology for shallow or deepwater applications, including data recovery from seafloor instruments and tether-free subsea vehicle control [1]. However, underwater environments are among the most complex wireless communication channels, and communication techniques using acoustic [2], [3], electromagnetic [4], and optical [5], [6] waves have emerged to tackle the fundamental and practical challenges of underwater wireless communications.

Among these technologies, underwater visible light communication (VLC) has attracted considerable interest over the past few years, since it offers high data rates and low latency within the optical range (<100 m) [5], [6]. Figure 1(a) shows a block diagram of underwater VLC systems, and Table 1 summarizes the existing underwater VLC systems. As the figure shows, the transmitter (Tx) modulates the message and emits the signal from light sources. The receiver (Rx) captures the signal using an optical detector and deciphers the message by demodulation. However, an underwater optical channel imposes challenges on the design of VLC systems, since it is characterized by high absorption of signals, scattering due to the particles present in the sea [7], and the existence of very shallow high ambient light conditions, resulting in low signal-to-noise ratio (SNR) environments.

To address these issues, the recent trend is to optimize optics systems. Existing VLC systems employ narrow beam laser diodes (LDs) and avalanche photodiodes (APDs) with a lens system as the light source and an optical detector,

The associate editor coordinating the review of this manuscript and approving it for publication was Jiajie Fan.

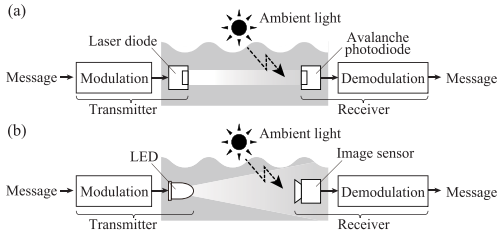

FIGURE 1. Block diagram of VLC system using: (a) laser diode and avalanche photodiode and (b) LED and image sensor.

TABLE 1. Existing underwater VLC systems.

Source	Destination	Modulation	Distance	Speed	Ref.
Laser diode (LD)	Avalanche photodiode (APD)	NRZ-OOK	7 m	2.3 Gbps	[10]
		PSK/QAM	64 m	5 Gbps	[11]
			8 m	1 Gbps	
		QAM-OFDM	5.4 m	4.8 Gbps	[12]
		OAM-OOK	2.96 m	3 Gbps	[13]
		OOK	20 m	1.5 Gbps	[14]
		OFDM	1.7 m	14.8 Gbps	[15]
		NRZ-OOK	34.5 m	2.7 Gbps	[16]
		OFDM	21 m	5.5 Gbps	[17]

respectively, to achieve a higher SNR. Various modulation techniques are also considered to maximize system performance, as summarized in Table 1.

However, the use of LED and image sensors in underwater VLC systems, as shown in Fig. 1(b), has not well been considered even though such systems have become famous applications in terrestrial indoor environments [8]. Since shallow or deepwater applications and subsea vehicles have powerful LED lighting systems working with camera systems [9], underwater VLC systems utilizing such existing components will become viable alternatives. However, two barriers exist: (1) the limited speed of the image sensor (image sensor: 30 – 60 Hz; APD: several GHz) and (2) underwater environments with high ambient light conditions. To address (1), the use of an LED array or a rolling-shutter sensor (*e.g.*, a CMOS image sensor) has been found to be effective in terrestrial indoor applications [18], [19], and both have been considered for use in underwater VLC systems [20], [21]. However, regarding (2), optimal signal modulation techniques suitable for underwater environments including "high ambient light" conditions have not been clarified yet, since high SNR conditions are available in VLC systems in terrestrial indoor environments.

Hence, in this paper we propose an underwater VLC system using a rolling-shutter sensor and reveal suitable modulation techniques for it through simulations and experiments. Section II describes an overview of the underwater VLC system using the rolling-shutter sensor as well as each modulation technique. Section III explains the characteristics of the channel and considers optimal modulation techniques. Section IV discusses simulations and their results. Section V discusses preliminary experiments in a small test tank and compares the results to those in Section IV. Section VI describes experiments in a large test tank with a wave generator and ambient light, and discusses the results. Section VII concludes this work.

II. SYSTEM OVERVIEW

Figure 2 shows a block diagram of the underwater VLC system using a rolling-shutter sensor. We assume that Tx and Rx are not synchronized and that the Tx knows the frame time T_f and the frame interval T_c of the rolling-shutter sensor at the Rx prior to communication. Under such conditions, a block transmission scheme – where a group of data is transmitted as a block with a header – is commonly employed [19], [23]. Specifically, the Tx reads binary data, performs modulation, adds a header on the modulated signal block, and emits the signal block from an LED. The Rx captures an image using a rolling-shutter sensor, converts the captured image to the signal by image processing, and performs signal block detection and demodulation. Below, we explain signal processing in the Tx and Rx in detail.

A. TRANSMITTER

Figure 3(a) shows the structure of a transmitted signal. Let us define a binary data block $\boldsymbol{b}_l = (b_{l,0}, b_{l,1}, \ldots, b_{l,N-1})$, where $b_{l,n} = \{0, 1\}, l = 0, 1, \ldots, L-1, n = 0, 1, \ldots, N-1$, l is the block number, L is the total number of data blocks, and N is the block length. The Tx reads $\boldsymbol{b}_l$ and calculates a payload signal $p_l(t')$ $(0 \leq t' \leq T_\mathrm{d})$ by performing modulation to $\boldsymbol{b}_l$ (we will employ several modulation techniques, as described in Section II-C). Then the Tx calculates a signal block $s_l(t')$ $(-T_\mathrm{h} \leq t' \leq T_\mathrm{d})$ by adding a header of length T_h (a known sequence of data used to identify the start of a data block) on $p_l(t')$. Finally, the Tx emits a signal $m(t)$, where the signal block $s_l(t')$ is repeated several times, as a fast-blinking light from the LED.

As noted above, the Tx emits the signal block repeatedly several times, because we have to consider two parameters – frame interval T_c and frame time T_f – to utilize the rolling-shutter sensor for the VLC system [Fig. 3(b)]. Unlike APDs that can capture incoming light continuously, a rolling-shutter sensor captures incoming light and outputs the image with an interval of T_c. However, the rolling-shutter sensor is active only for the time of T_f $(T_\mathrm{f} < T_\mathrm{c})$ during this interval, because a blind time of $T_\mathrm{c} - T_\mathrm{f}$ is required to read out the image. To address this issue without Tx-Rx synchronization, the length of the signal block $T_\mathrm{b} = T_\mathrm{h} + T_\mathrm{d}$ should be $T_\mathrm{b} \leqq T_\mathrm{f}/2$ and $T_\mathrm{b} = T_\mathrm{c}/U$ (U is a positive integer and $U \geqq 3$), and it should be transmitted repeatedly U times so that the rolling-shutter sensor can capture at least one signal block successfully [Fig. 3(b)]. Consequently, the signal $m(t)$ can be expressed as

$$\begin{aligned} m(t) &= s_{\lfloor \frac{u}{U} \rfloor}(t') \\ &= s_{\lfloor \frac{u}{U} \rfloor}(t - uT_\mathrm{b}) \end{aligned}$$

where u is the total number of transmitted signal blocks (L signal blocks are repeated U times) and $u = 0, 1, \ldots, UL-1$.

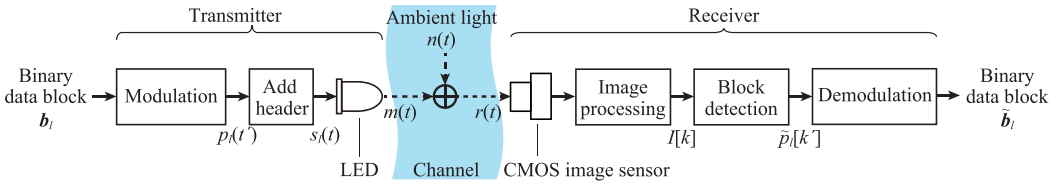

FIGURE 2. Block diagram of underwater VLC system using the rolling-shutter of a CMOS image sensor.

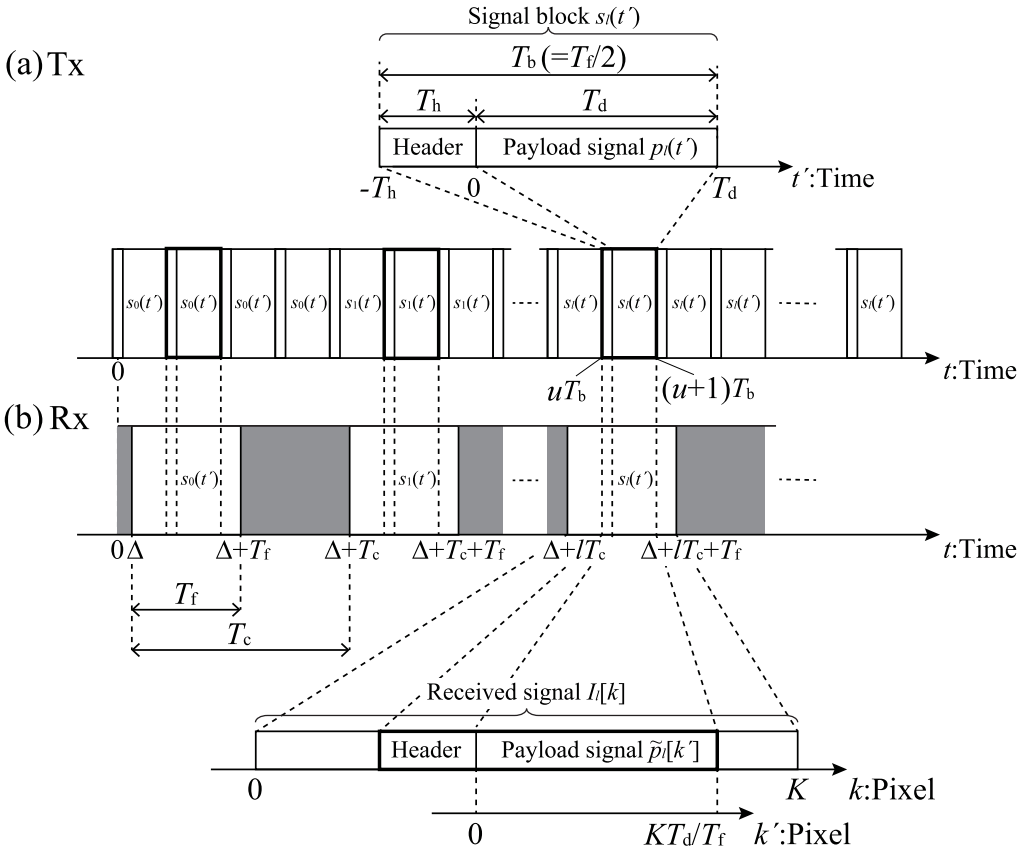

FIGURE 3. Structure of (a) transmitted signal and that of (b) received signal. Relationship between signal block length, frame time T_f, and frame interval T_c of CMOS image sensor when $T_c = 2T_f$ and $U = 4$ is illustrated.

B. RECEIVER

The Rx captures the incoming light $r(t) = m(t) + n(t)$ [$n(t)$ represents ambient light] as images using the rolling-shutter sensor, and converts the images to the signal $I_l[k]$. We assume that $I_l[k]$ contains information of the l-th signal block $s_l(t)$.

Figure 4 shows the relationships among the exposure time of the rolling-shutter sensor, the output image, and the received signal $I_l[k]$. We assume that the rolling-shutter sensor has K image rows. In the rolling-shutter sensor, the start and end of exposure on each row, column, or individual pixel happens sequentially. Hence, if the sensor captures a fast-blinking light, the light would be observed as light and dark stripes, as shown in the figure. In other words, the rolling-shutter sensor has a function that converts fast-blinking light in the time domain to that in the space domain (K rows are scanned by the total time gaps between row-by-row scans T_e). In this case, the luminescence of the captured image at the k-th row ($k = 0, 1, \ldots, K-1$) can be expressed as

$$\begin{aligned} I_l[k] &= \int_{\Delta+lT_c+\frac{k}{K}T_e}^{\Delta+lT_c+\frac{k}{K}T_e+\alpha T_f} r(t)dt \\ &\simeq r(\tilde{k})\alpha T_f \\ &= \alpha T_f(m(\tilde{k}) + n(\tilde{k})), \end{aligned} \tag{1}$$

where

$$\tilde{k} = \Delta + lT_c + \frac{k}{K}T_e,$$

and α and Δ are the ratio of the exposure time of each image row to the frame time (αT_f: exposure time of each

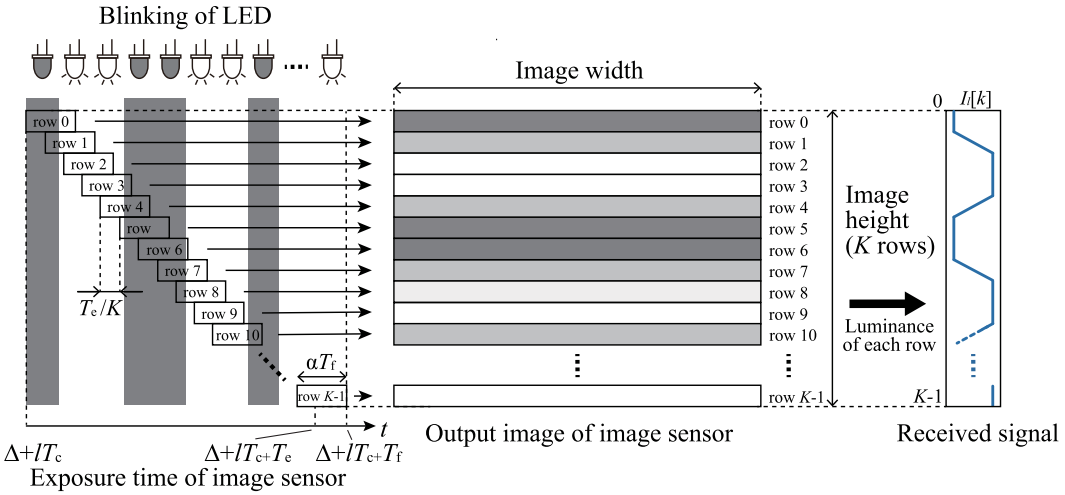

FIGURE 4. Relationships among exposure timing of rolling-shutter sensor, output image, and received signal.

image row) and the time gap between the transmitter and the receiver, respectively. As shown in (1), the output of the rolling-shutter sensor $I_l[k]$ (the luminance of each row) becomes a discretized signal of $m(t)$ with optical noise $n(t)$.

Then the Rx obtains a payload signal $\tilde{p}_l[k']$ ($0 \leq k' \leq KT_d/T_f$) by detecting a header on $I_l[k]$. As shown in Fig. 3, the length of the payload signal can be expressed as T_d and KT_d/T_f in the time and space (pixel) domains, respectively, and

$$k' = \frac{K}{T_f} t'.$$

Hence, the received payload signal $\tilde{p}_l[k']$ can be expressed as

$$\begin{aligned} \tilde{p}_l[k'] &\simeq p_l(t') + n(t') \\ &= p_l\left[\frac{T_f}{K}k'\right] + n\left[\frac{T_f}{K}k'\right]. \end{aligned} \tag{2}$$

As shown in (2), the received payload signal block $\tilde{p}_l[k']$ becomes the sum of the transmitted payload signal block $p_l(t')$ and the optical noise $n(t')$. Finally, the Rx obtains binary data block $\tilde{\boldsymbol{b}}_l$ by performing demodulation to $\tilde{p}_l[k']$.

C. MODULATION TECHNIQUES

In this paper, we reveal suitable modulation techniques for an underwater VLC system using a rolling-shutter sensor, as described in Sections II-A and II-B. Specifically, we consider three types of modulation techniques: (a) PSK, (b) NRZ-OOK [10], and (c) OFDM [15]. Note that the first technique (a) is introduced for an underwater VLC system for the first time in this paper.

Figures 5(a)-5(c) show the equation, waveform, and spectrum of payload signal $p_l(t')$ using each modulation technique.

- (a) In PSK, the phase of the signal operating at frequency f_c changes between discrete levels in time in accordance with the binary data $b_{l,n}$. A typical equation of the payload signal $p_l(t')$, its waveform, and its spectrum are shown in Fig. 5(a). As the figure shows, the envelope of the signal waveform is constant and the spectrum of the signal is located in a relatively high-frequency regime whose center is located at f_c. The PSK signal can be demodulated by performing frequency downconversion and applying a specific threshold to the baseband (converted) signal.
- (b) In NRZ-OOK, the signal amplitude changes between discrete levels in time in accordance with the binary data $b_{l,n}$. A typical equation of the payload signal $p_l(t')$, its waveform, and its spectrum are shown in Fig. 5(b), where a and a_{off} are the signal amplitude and the DC offset to make $p_l(t')$ positive, respectively. As the figure shows, the signal amplitude has only two levels and the spectrum of the signal is located in a low-frequency regime. The NRZ-OOK signal can be demodulated by applying a specific threshold to the received signal. It has been found that the choice of threshold settings is critical to the performance of the receiver, and that the use of an adaptive threshold is effective to ensure an optimal threshold setting [23].
- (c) In OFDM, the signal becomes the sum of several signals operating at different frequencies (*i.e.*, subcarriers) whose phase represents the binary data $b_{l,n}$. A typical equation of the payload signal $p_l(t')$, its waveform, and its spectrum are shown in Fig. 5(c). As the figure shows, the signal amplitude changes dynamically, resulting in a high peak-to-average power ratio (PAPR) [24], and the spectrum of the signal is located in a relatively high-frequency regime as well as that of PSK. The OFDM signal can be demodulated by performing frequency downconversion and a fast Fourier transform on the received signal and measuring the phase of each subcarrier.

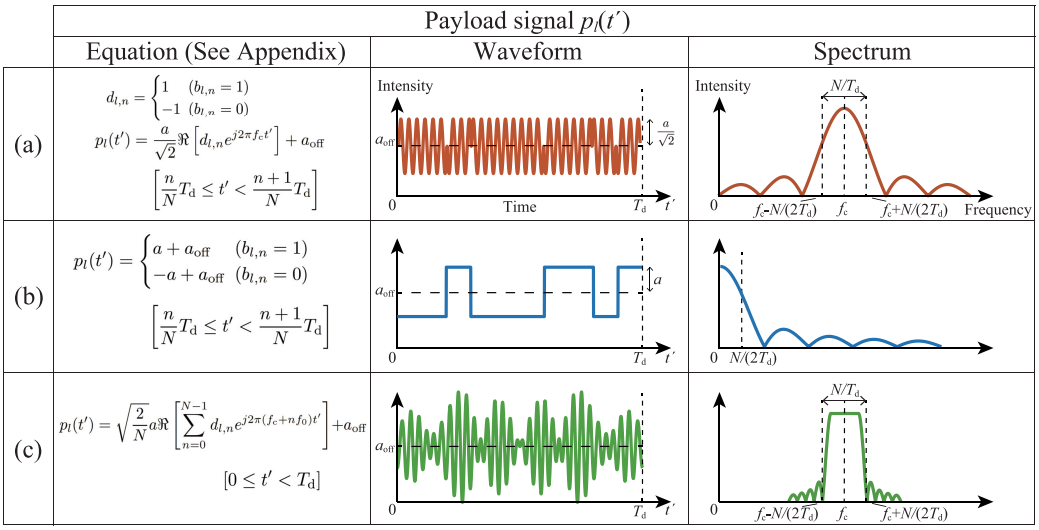

FIGURE 5. Equation, waveform, and spectrum of payload signal $p_l(t')$ using each modulation technique: (a) PSK, (b) NRZ-OOK, and (c) OFDM.

In the following simulations and experiments, we compare the performance of these modulation techniques under the same conditions. Specifically, we set the parameters so that the total power of payload signal $E[p_l^2(t')]$, the signal bandwidth N/T_d, and the DC offset a_{off} are equal among all modulation techniques. First, however, in the next section we discuss the advantages and disadvantages of these modulation techniques applied to an underwater VLC system using a rolling-shutter sensor.

III. CHARACTERISTICS OF THE CHANNEL AND OPTIMAL MODULATION TECHNIQUES

As shown in Fig. 1(b), to achieve a reliable underwater VLC system using a rolling-shutter sensor in an underwater channel including high ambient light conditions, we have to consider two characteristics of the channel and sensor – (A) interference of ambient light, and (B) pixel saturation. Below we discuss these characteristics and reveal the optimal modulation technique.

A. PROBLEM: INTERFERENCE OF AMBIENT LIGHT

As shown in Fig. 1, ambient light (*e.g.*, daylight) is scattered by a surface wave (typical frequency: <1 Hz [25]) and reaches the Rx. Hence, the underwater ambient light $n(t)$ in Fig. 2 appears in the low-frequency regime, and the noise in the received signal (observed by the rolling-shutter sensor) also appears in the low spatial frequency regime (note that the rolling-shutter sensor has a function that converts a signal in the time domain to the space (pixel) domain).

Figures 6(a) and 6(b) show the spectra of the received payload signal $\tilde{p}_l[k']$ using the baseband modulation technique (NRZ-OOK) and the passband modulation technique (PSK and OFDM), respectively. As the figure shows, when we employ the baseband modulation technique [Fig. 6(a)], interference occurs between the signal (blue line) and ambient light (red line), which becomes a barrier to achieving reliable communication in very shallow high ambient light conditions. On the other hand, the use of the passband modulation technique [Fig. 6(b)] would be preferable, since the spectrum of the signal and that of ambient light components appear in different spatial frequency regimes if we design the carrier frequency f_c carefully. In this case, we can avoid signal-to-noise interference by applying a bandpass filter on the received signal $\tilde{p}_l[k']$.

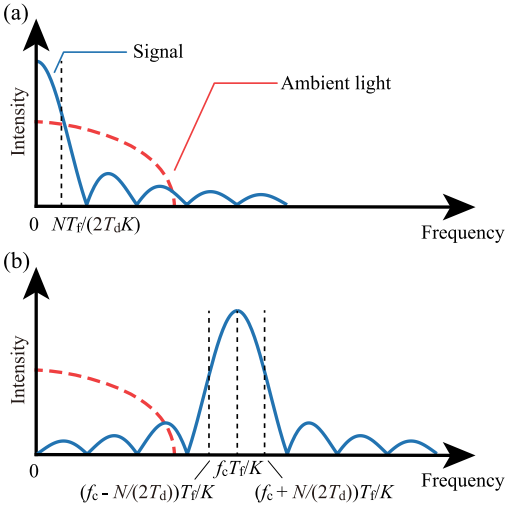

FIGURE 6. Relationship between spectrum of ambient light and received payload signal $\tilde{p}_l[k']$ using: (a) baseband modulation techniques and (b) passband modulation techniques.

B. PROBLEM: PIXEL SATURATION

Since ambient light changes dynamically in an underwater environment, there is a concern that pixels become saturated

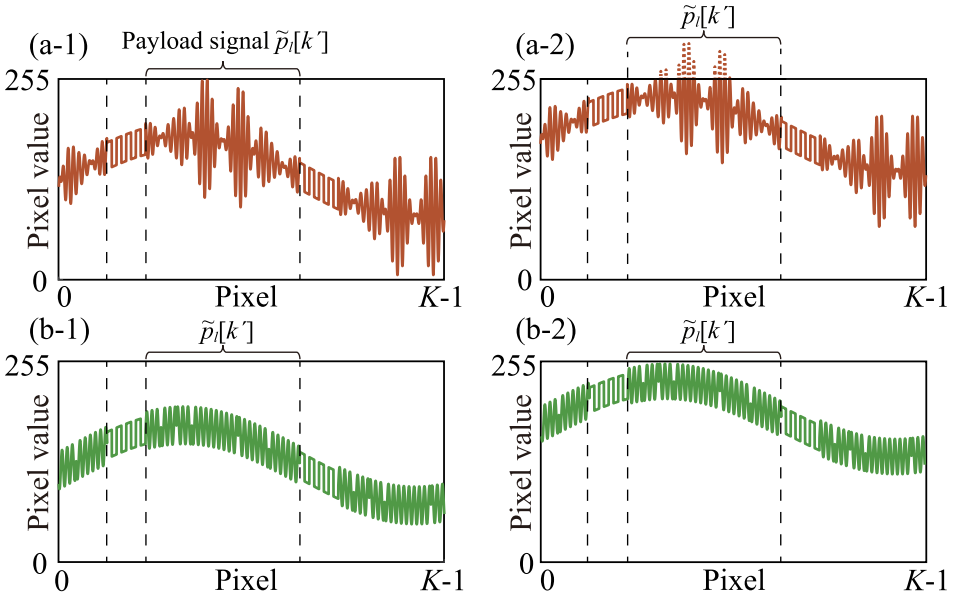

FIGURE 7. Example of waveform of received payload signal $\tilde{p}_l[k']$ using (a-1) OFDM, (b-1) PSK, (a-2) OFDM (in high ambient light condition), and (b-2) PSK (in high ambient light condition).

when the intensity of ambient light jumps and exceeds a threshold, resulting in an increase in BER.

As shown in Figs. 7(a-1) and 7(b-1), to achieve the best possible signal resolution, the input signal should be maximized across the dynamic range of the rolling-shutter sensor. However, the pixel saturation – a nonlinear distortion where the recorded image is limited to some maximum value – occurs when the intensity of ambient light increases, resulting in interference with the measurement of signal amplitude. Such nonlinear distortion, which can significantly increase BER, is more likely to occur when the PAPR of the signal is high, as shown in Figs. 7(a-2) and 7(b-2). Hence, the use of NRZ-OOK and PSK would be preferable since the PAPR of NRZ-OOK and that of PSK are smaller than that of OFDM.

C. DISCUSSION: OPTIMAL MODULATION

Table 2 summarizes the characteristics of the channel and modulation techniques based on the above discussion. As the table shows, when the two characteristics of the channel are considered, PSK modulation is considered the optimal modulation technique in an underwater channel with high ambient light conditions.

In Section III-A, we illustrate that passband modulation techniques (PSK and OFDM) would be preferable in an underwater channel with low-frequency ambient light scattered by a surface wave, since these modulation techniques can avoid signal-to-noise interference if we carefully design carrier frequency f_c to be between the frequency of the ambient light and the sampling frequency of the rolling-shutter sensor (theoretically K/T_f) (Table 2, column 1).

In Section III-B, we illustrate that low-PAPR modulation techniques (PSK and NRZ-OOK) would be preferable in an underwater channel with dynamically changing intensity of ambient light since these modulation techniques are less likely to lead to pixel saturation compared to the high-PAPR modulation technique (OFDM) (Table 2, column 2).

TABLE 2. Classification of the modulation techniques [(a) PSK, (b) NRZ-OOK, and (c) OFDM] based on the characteristics of the channel [A. interference of ambient light and B. pixel saturation].

	A. Interference of ambient light	B. Pixel saturation
(a) PSK	✓	✓
(b) NRZ-OOK		✓
(c) OFDM	✓	

Consequently, the optimal modulation technique for an underwater VLC system using a rolling-shutter sensor in environments with high ambient light conditions would be PSK modulation. In the following section, we perform simulations and experiments as in previous studies of underwater VLC [10]–[23], and reveal the effectiveness of PSK modulation in an underwater channel. Note that an evaluation of the performance of the communication system using theoretical equations is outside the scope of this paper, since a precise model of the complex underwater communication channel is necessary.

IV. SIMULATION

In this section we perform computer simulations of a VLC system using a rolling-shutter sensor and each modulation technique (PSK, NRZ-OOK, and OFDM), considering two characteristics (A. interference of ambient light and B. pixel

TABLE 3. Parameters used in the simulation.

Transmitter	Sampling frequency	240 kHz
	Number of bits per block N	10 bits
	Length of signal block T_b	1/120 s
	Length of header T_h	1/600 s
	Length of data block T_d	1/150 s
	Carrier frequency f_c	4.5 kHz
	Number of repetitions of signal block U	4
	Number of subcarriers of OFDM signal block N	10
	Amplitude of signal block a	0.18^*
	DC offset of signal block a_{off}	0.43^* (Sec. IV-A) 0.81^* (Sec. IV-B)
	Effective data rate	300 bps
Receiver	Sampling frequency K/T_f	54 kHz
	Frame time T_f	1/60 s
	Frame rate $1/T_c$	30 fps
	Ratio of exposure time of each image row to frame time α	1
	Image rows K	900
Noise	Frequency f_n	$0-10.0$ Hz (Sec. IV-A) 0 Hz (Sec. IV-B)
	DC offset n_{off}	0.18^* (Sec. IV-A) $0-1^*$ (Sec. IV-B)
	Amplitude a_n	0.18^* (Sec. IV-A) 0^* (Sec. IV-B)

* These parameters are normalized by the maximum value (saturation level).

saturation). The following simulations are performed on computer software (MATLAB, MathWorks).

A. RESILIENCE OF EACH MODULATION TECHNIQUE TO INTERFERENCE OF AMBIENT LIGHT

1) SYSTEM SETUP

In this simulation, we evaluate the underwater VLC system using each modulation technique in a channel with low-frequency ambient light as described in Section III-A. Table 3 shows the parameters used in the simulation. We calculate a payload signal $p_l(t')$, a transmission signal $m(t)$, and noise (ambient light) $n(t)$ using these parameters. Figures 8(a), 8(b), and 8(c) show examples of signal blocks using PSK, NRZ-OOK, and OFDM, respectively. We then calculate the received signal $I_l[k]$, obtain a payload signal $\tilde{p}_l[k']$, perform demodulation, and calculate SNR and BER by changing the frequency of $n(t)$, f_n. Note that the noise (ambient light) is assumed to be a sinusoidal signal with amplitude a_n and offset n_{off}, and the received signal $I_l[k]$ is calculated by resampling $m(t)+n(t)$ with a sampling rate of K/T_f (conversion from the sampling frequency of the transmitted signal in the time domain to that of the received signal in the space (pixel) domain, as described in Section II-B).

2) RESULTS AND DISCUSSION

Figure 9 shows the simulation results. Figures 9(a) and 9(b) show the relationship between the ambient light frequency f_n and SNR and that between the ambient light frequency f_n and BER, respectively. The red, blue, and green lines represent the results of PSK, NRZ-OOK, and OFDM, respectively. As shown in Fig. 9(a), we found that the SNR of the VLC system using PSK, NRZ-OOK, and OFDM were almost the same at each f_n. Therefore, PSK, NRZ-OOK, and OFDM all showed comparable performance at each f_n.

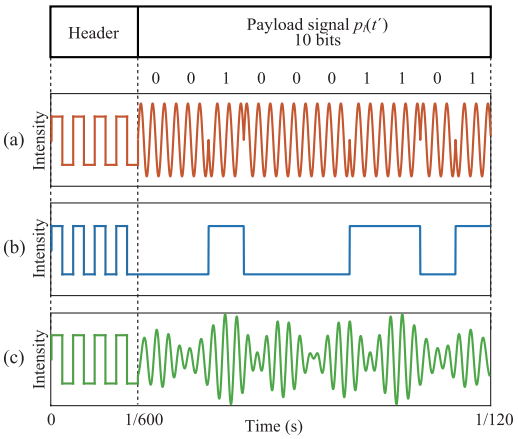

FIGURE 8. Examples of transmitted signal block $p_l(t')$ using: (a) PSK, (b) NRZ-OOK, and (c) OFDM.

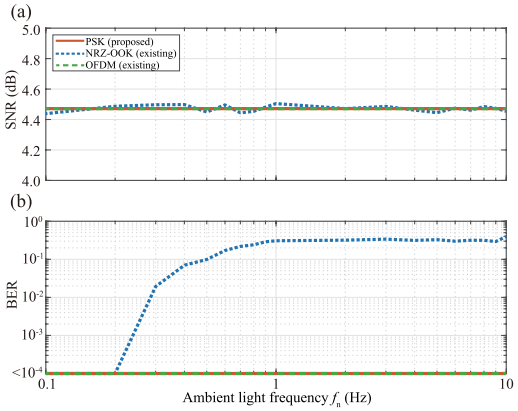

FIGURE 9. Simulation results to evaluate the resilience of each modulation technique to interference of ambient light: (a) relationship between the ambient light frequency f_n and SNR and (b) relationship between the ambient light frequency f_n and BER.

As shown in Fig. 9(b), the BERs of PSK, NRZ-OOK, and OFDM are each less than 10^{-4} when $f_n \leq 0.2$. On the other hand, the BER of NRZ-OOK increases when $f_n > 0.2$, while those of PSK and OFDM remain less than 10^{-4}. This is because the intensity of the received NRZ-OOK signal changes dynamically within a short time (less than the signal block duration T_b), making it difficult for the Rx to determine an optimal threshold. In contrast, the effect of ambient light can be avoided in the PSK and OFDM, as described in Section III-A. These results suggest that the VLC system using PSK or OFDM outperforms that using NRZ-OOK in an underwater environment with low-frequency ambient light.

B. TOLERANCE OF EACH MODULATION TECHNIQUE TO PIXEL SATURATION

1) SYSTEM SETUP

In this simulation, we evaluate the underwater VLC system using each modulation technique in a channel with high ambient light, resulting in pixel saturation, as described in

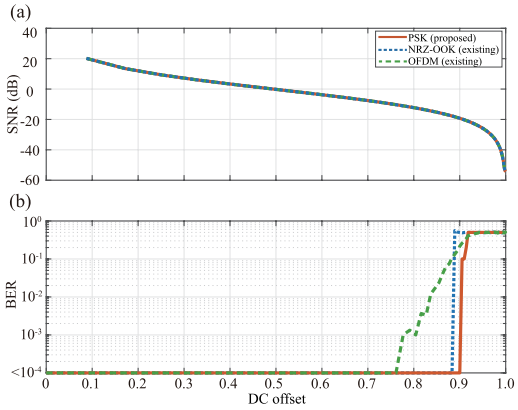

FIGURE 10. Simulation results to evaluate the tolerance of each modulation technique to pixel saturation: (a) relationship between DC offset and SNR and (b) relationship between DC offset and BER.

Section III-B. As with the previous simulation, we used the parameters summarized in Table 3. We calculate a payload signal $p_l(t')$, a transmission signal $m(t)$, and noise (DC offset) $n(t)$ using these parameters. Then we calculate the received signal $I_l[k]$, obtain a payload signal $\tilde{p}_l[k']$, perform demodulation, and calculate SNR and BER by changing the DC offset of $n(t)$.

2) RESULTS AND DISCUSSION

Figure 10 shows the simulation results. Figures 10(a) and 10(b) show the relationship between the DC offset and the SNR and that between the DC offset and the BER, respectively. The red, blue, and green lines represent the results of PSK, NRZ-OOK, and OFDM, respectively. As shown in Fig. 10(a), we found that the SNR of the VLC system using PSK was almost the same as that using NRZ-OOK at each DC offset. Therefore, PSK, NRZ-OOK, and OFDM showed comparable performance at each DC offset.

As shown in Fig. 10(b), the BER of the VLC system using OFDM increases when the DC offset is more than 0.76, while the BER of NRZ-OOK and that of PSK each remain less than 10^{-4}. This is because the OFDM signal, which has high PAPR, causes pixel saturation in high ambient light conditions before NRZ-OOK and PSK do, as described in Section III-B. These results suggest that the VLC system using PSK or NRZ-OOK outperforms that using OFDM in very shallow high ambient light conditions.

V. PRELIMINARY EXPERIMENT

To validate the simulation results (Section IV), we conduct a preliminary experiment using the VLC system with PSK, NRZ-OOK, and OFDM in a small test tank.

A. RESILIENCE OF EACH MODULATION TECHNIQUE TO INTERFERENCE OF AMBIENT LIGHT

1) SYSTEM SETUP

The preliminary experiment was performed using a small test tank in a dark room, as shown in Fig. 11. The Tx consisted of

TABLE 4. Parameters used in the experiment.

Transmitter	Sampling frequency	240 kHz
	Number of bits per block N	10 bits
	Length of signal block T_b	1/120 s
	Length of header T_h	1/600 s
	Length of data block T_d	1/150 s
	Carrier frequency f_c	4.5 kHz
	Number of repetitions of signal block U	4
	Number of subcarriers of OFDM signal block N	10
	Amplitude of signal block a	0.18^*
	DC offset of signal block a_off	0.43^* (Sec. IV-A) 0.81^* (Sec. IV-B)
	Effective data rate	300 bps
Receiver	Frame time T_f	1/60 s
	Frame rate $1/T_\mathrm{c}$	30 fps
	Image rows	900
Ambient light source	Frequency f_n	$0-10.0$ Hz (Sec. IV-A) 0 Hz (Sec. IV-B)
	DC offset n_off	0.18^* (Sec. IV-A) $0-1^*$ (Sec. IV-B)
	Amplitude a_n	0.18^* (Sec. IV-A) 0^* (Sec. IV-B)

* These parameters are normalized by the maximum value (saturation level).

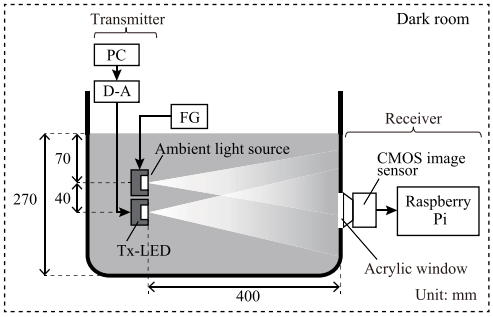

FIGURE 11. Experimental environment using a small test tank.

a personal computer with software (MATLAB, MathWorks), a digital-to-analog (D-A) converter (USB-6363; National Instruments), and a blue LED (OSB5XME3C1E; OptoSupply) with a lens (OSOLRA2045M; OptoSupply). The Rx consisted of a rolling-shutter sensor (Raspberry Pi Camera Module V2) and a microcomputer (Raspberry Pi). Another blue LED (OSB5XME3C1E; OptoSupply) with a lens connected to a function generator (FG) (DF1905; NF Corporation) was used as the ambient light source. As shown in the figure, the distance between Tx and Rx is the same as that between the ambient light source and Rx.

Table 4 shows the parameters used in the experiment. Tx calculates the signal $m(t)$ and emits the signal from the LED. At the same time, the ambient light source emits the sinusoidal signal with a frequency f_n of 0 – 10 Hz as $n(t)$. The Rx captures the signal and ambient light using the rolling-shutter sensor, performs demodulation, and calculates SNR and BER at each f_n.

2) RESULTS AND DISCUSSION

Figure 12 shows the preliminary experimental results. Figures 12(a) and 12(b) show the relationship between the ambient light frequency f_n and SNR and that between the ambient light frequency f_n and BER, respectively. The red,

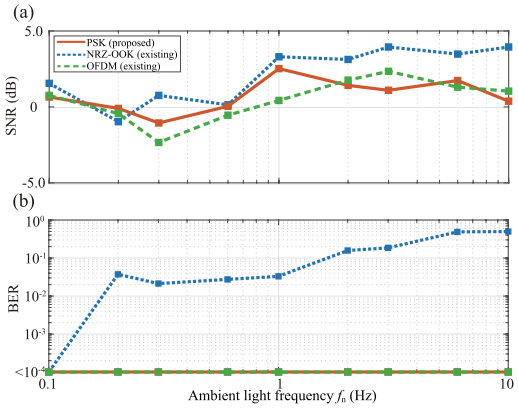

FIGURE 12. Preliminary experimental results for the resilience of each modulation technique to interference of ambient light: (a) relationship between the ambient light frequency f_n and SNR and (b) relationship between the ambient light frequency f_n and BER.

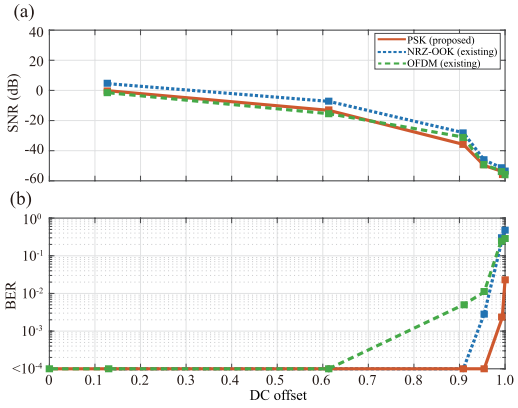

FIGURE 13. Preliminary experimental results to evaluate tolerance of each modulation technique to pixel saturation: (a) relationship between DC offset and SNR and (b) relationship between DC offset and BER.

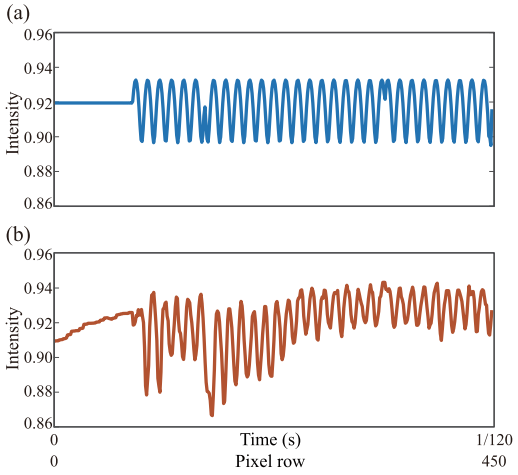

FIGURE 14. Example of the received signal block in the: (a) simulation, and (b) preliminary experiment.

blue, and green lines represent the results of PSK, NRZ-OOK and OFDM, respectively. As shown in Fig. 12(a), the SNR varied from -2.3 to 3.9 (dB) as f_n changed. Furthermore, SNR values of PSK, NRZ-OOK, and OFDM were different (the maximum difference was 3.9 dB when $f_n = 10$), although the power of noise and the PSK, NRZ-OOK, and OFDM signals input to the LED were the same. The difference might be attributable to the LED luminance changing as the operating frequency changes. (Basically, the luminance of the LED tends to decrease as the operating frequency increases). However, it is reasonable to compare the performances of PSK, NRZ-OOK, and OFDM under the same input signal power.

As shown in Fig. 12(b), the BERs of PSK, NRZ-OOK, and OFDM are each less than 10^{-4} when $f_n = 0.1$. On the other hand, the BER of NRZ-OOK increases when $f_n = 0.2 - 10$, while that of PSK or OFDM remains less than 10^{-4}. Therefore, as in Section IV-A, we confirmed that the VLC system using PSK or OFDM avoided low-frequency ambient light in the experiment as well as in the simulation.

B. TOLERANCE OF EACH MODULATION TECHNIQUE TO PIXEL SATURATION

1) SYSTEM SETUP

We also evaluate the tolerance of each modulation technique to pixel saturation. The experimental environment and the configuration of Tx and Rx are the same as those in Section V-A. As in the previous experiment, we used the parameters summarized in Table 4. In this experiment, Tx emits the signal $m(t)$, and the ambient light source emits DC offset as $n(t)$. The Rx captures the signal and ambient light, performs demodulation, and calculates SNR and BER for each DC offset level.

2) RESULTS AND DISCUSSION

Figure 13 shows the preliminary experimental results. Figures 13(a) and 13(b) show the relationship between the DC offset of ambient light and SNR and that between the DC offset of ambient light and BER, respectively. The red, blue, and green lines represent the results for PSK, NRZ-OOK, and OFDM, respectively. As shown in Fig. 13(a), the SNR values of PSK, NRZ-OOK, and OFDM were different (the maximum difference was 8.2 dB when DC offset was 0.61), although the power of noise and PSK, NRZ-OOK, and OFDM signals input to the LED were the same, as shown in Section V-A. However, it is reasonable to compare the performances of PSK, NRZ-OOK, and OFDM under the same input signal power.

As shown in Fig. 13(b), the BER of OFDM increases when the DC offset of ambient light is 0.91, while the BERs of NRZ-OOK and PSK remain less than 10^{-4}. These results support the simulation results.

However, the BERs of PSK and NRZ-OOK in the experiment increase more slowly than those in the simulation. This is because the received signal in the simulation is different from that in the experiment. Figure 14 shows an example

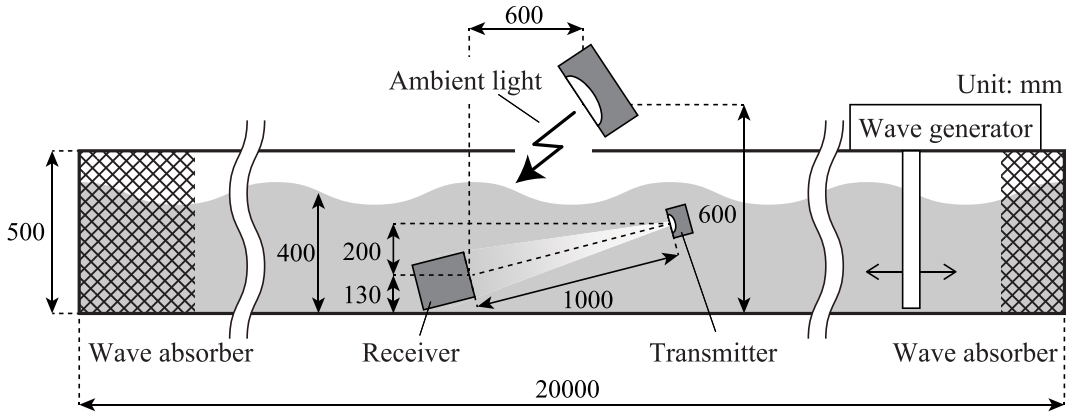

FIGURE 15. Experimental environment using a large test tank with a wave generator and ambient light.

of the received signal block. Figures 14(a) and 14(b) show examples of a received signal using PSK obtained in the simulation and that obtained in the experiment, respectively. As shown in Fig. 14(a), the received signal has a constant DC offset. Therefore, in the cases of PSK and NRZ-OOK, which have constant amplitudes, BER increases rapidly when the DC offset reaches the threshold value, as shown in Fig. 10(b).

On the other hand, in the experiment, neither the DC offset nor the amplitude of the received signal is constant [Fig. 14(b)], although the power of the noise input and that of the signal input to the LED were the same as in the simulation. A possible reason for this is that the distribution of luminance on the rolling-shutter sensor is not constant, since the sensor obtains the signal from the image. Therefore, when the DC offset increases, the pixels gradually become saturated and the BER slowly increases, as shown in Fig. 13(b).

Consequently, as in Section IV-B, we confirmed that the VLC system using PSK or NRZ-OOK outperformed that using OFDM in the experiment as well as in the simulation.

VI. PERFORMANCE EVALUATION OF THE PROPOSED SYSTEM

In this section we evaluate the performance of the VLC system using PSK, NRZ-OOK, and OFDM in experiments. The experimental environment is demonstrated in Section VI-A. In Section VI-B, we analyze the ambient light scattered by surface waves. In Section VI-C, we conduct experiments using a wave tank (a test tank with a wave generator and ambient light) and demonstrate the performance of the VLC system using each modulation technique.

A. SYSTEM SETUP

The experiment was performed using a large test tank, as shown in Figure 15. The configuration of Tx and Rx is shown in Figure 16. The Tx and Rx configurations were the same as those in the preliminary experiment (Section V). Unlike the case in the preliminary experiment, here a high-intensity discharge lamp (HCF1572BHE; Iwasaki Electric Co.) was used as an ambient light source.

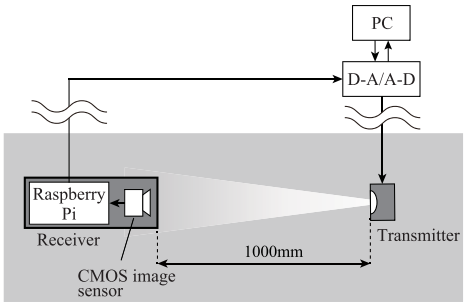

FIGURE 16. Configuration of Tx and Rx.

B. ANALYSIS OF AMBIENT LIGHT SCATTERED BY SURFACE WAVES

Before the experiments, we analyzed the ambient light scattered by surface waves [see Fig. 1(b)].

In this analysis, the wave generator generates surface waves with a frequency of $f_w = 0, 0.25, \ldots, 1$ (Hz) and with a height of $h_w = 0, 25, \ldots, 100$ (mm). The Tx is silent, and the ambient light source emits DC offset. The Rx captures only the ambient light scattered by the surface waves.

Figures 17(a)-(i) show the analysis results. Figures 17(a-1) - (i-1) illustrate the changes in the intensity of the received frame when there are surface waves. The blue and red lines represent the maximum and minimum pixel values of the received frame, respectively. The green lines represent examples of the received frame. The intensity of the received ambient light exists in the regime whose lower and upper bounds are red and blue lines, respectively. As can be seen in figures, the change in the intensity of the received ambient light increases in proportion to the wave height h_w and wave frequency f_w. As shown in Figs. 17(d-1), 17(e-1), and 17(i-1), when the wave height h_w or wave frequency f_w is high (Section III-B), the intensity of ambient light exceeds the threshold and pixel saturation occurs.

Figures 17(a-2) - (i-2) illustrate the power spectral density (PSD) of received ambient light. The sum of the PSD of each received frame is shown in the figure since the received

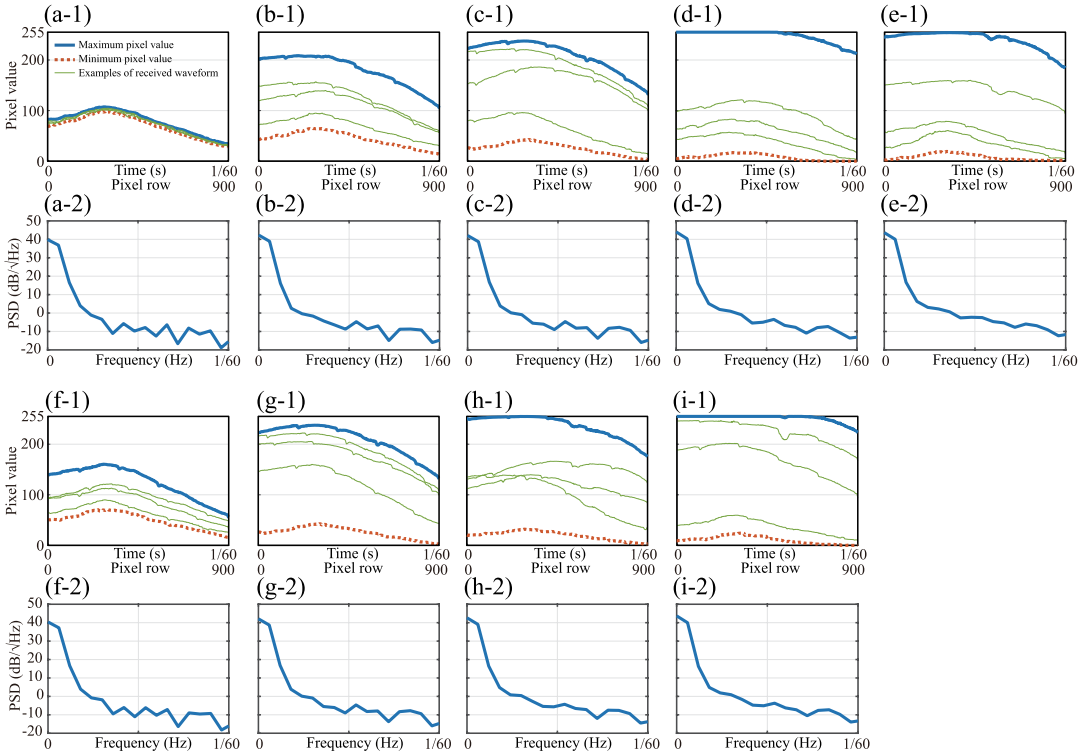

FIGURE 17. Changes in the intensity and power spectral density (PSD) of received frames: (a) wave height $h_w = 0$ mm, wave frequency $f_w = 0$ Hz; (b) $h_w = 50$ mm, $f_w = 0.25$ Hz; (c) $h_w = 50$ mm, $f_w = 0.5$ Hz; (d) $h_w = 50$ mm, $f_w = 0.75$ Hz; (e) $h_w = 50$ mm, $f_w = 1.0$ Hz; (f) $h_w = 25$ mm, $f_w = 0.5$ Hz; (g) $h_w = 50$ mm, $f_w = 0.5$ Hz; (h) $h_w = 75$ mm, $f_w = 0.5$ Hz; and (i) $h_w = 100$ mm, $f_w = 0.5$ Hz.

signal is not a continuous signal, as described in Section II-B. As the figures show, ambient light exists around the low-frequency regime. Hence, the obtained results suggest that we can avoid interference between the signal and ambient light if the carrier frequency is much higher than the ambient light frequency (Section III-A).

C. EXPERIMENTAL RESULTS AND DISCUSSION

We evaluate the performance of the VLC system using PSK, NRZ-OOK, and OFDM in a large test tank.

Table 5 shows the parameters used in the experiment. The wave generator generates surface waves with a frequency of $f_w = 0, 0.25, \ldots, 1$ (Hz) and with a height of $h_w = 0, 25, \ldots, 100$ (mm). The Tx emits the signal $m(t)$, and the ambient light source emits the DC offset as $n(t)$. The Rx captures the signal and ambient light scattered by the surface waves, performs demodulation, and calculates SNR and BER for each f_w and h_w.

Figure 18 shows the experimental results. Figures 18(a-1)-(d-1) and 18(e-1)-(h-1) show the relationship between the wave height h_w and SNR (fixed wave frequency f_w) and that between the wave frequency f_w and SNR (fixed wave height h_w), respectively. The red, blue, and green lines show the results for PSK, NRZ-OOK, and OFDM, respectively.

As shown in Figs. 18(a-1)-(h-1), the SNR varied from -11.2 to -3.1 (dB) as h_w and f_w changed, since the ambient light was scattered by surface waves. Furthermore, SNR of PSK, NRZ-OOK, and OFDM were different (the maximum difference was 7.0 dB when $h_w = 100$ and $f_w = 0.75$), although the power of noise and the PSK, NRZ-OOK, and OFDM signals input to the LED were the same. A possible reason for this is that the LED luminance changes as the operating frequency changes, as shown in Section V-A. However, it is reasonable to compare the performances of PSK, NRZ-OOK, and OFDM under the same input signal power.

TABLE 5. Parameters used in the experiment.

Trans-mitter	Sampling frequency	240 kHz
	Number of bits per block N	10 bits
	Length of signal block $T_f/2$	1/120 s
	Length of header	1/600 s
	Length of data block	1/150 s
	Carrier frequency f_c	4.5 kHz
	Number of repetitions of signal block U	4
	Number of subcarriers of OFDM signal block N	10
	Amplitude of signal block a	0.3 V
	DC offset of signal block a_{off}	1.4 V
	Effective data rate	300 bps
Receiver	Frame time T_f	1/60 s
	Frame rate $1/T_c$	30 fps
	Image rows	900
Wave	Wave frequency f_w	$0 - 1.0$ Hz
	Wave height h_w	$0 - 100$ mm

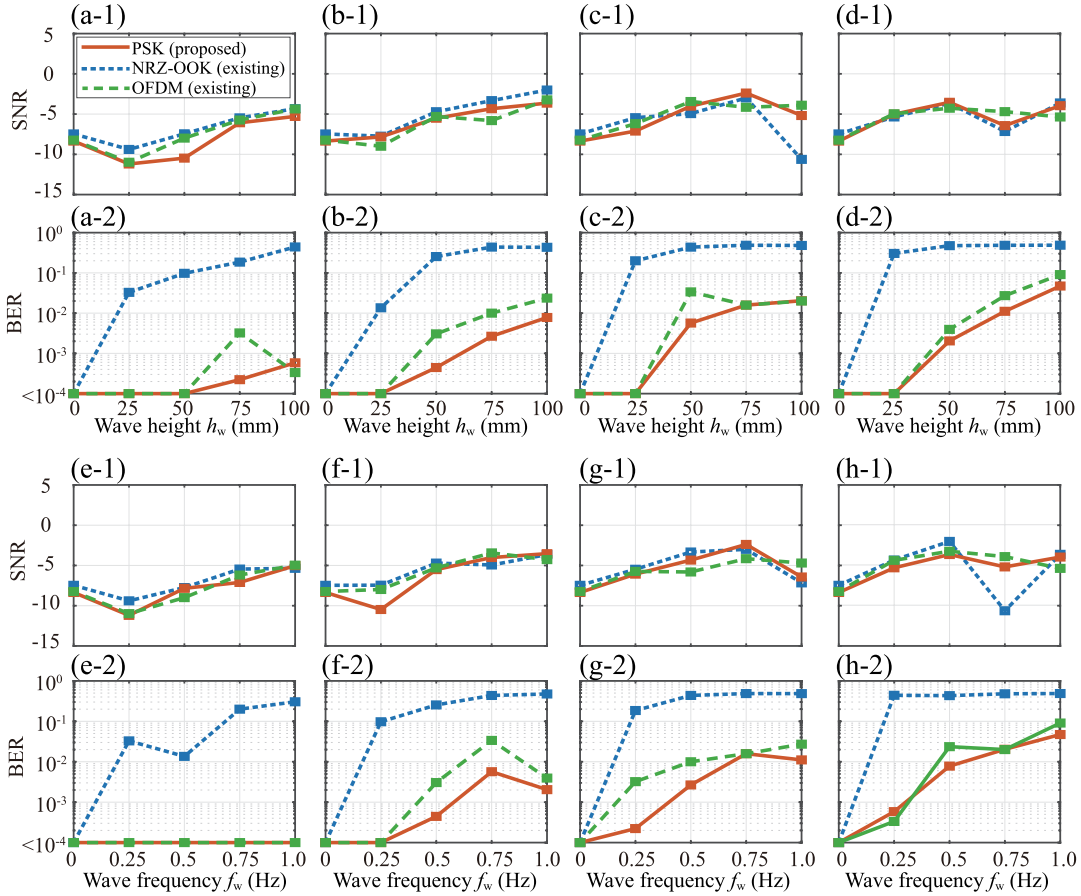

FIGURE 18. Experiment results to evaluate resilience of each modulation technique in environment including "high ambient light" conditions; relationship between wave height h_w, SNR, and BER when (a) $f_w = 0.25$ Hz, (b) $f_w = 0.5$ Hz, (c) $f_w = 0.75$ Hz, and (d) $f_w = 1$ Hz, and relationship between wave frequency f_w, SNR, and BER when (e) $h_w = 25$ mm, (f) $h_w = 50$ mm, (g) $h_w = 75$ mm, and (h) $h_w = 100$ mm.

Figures 18(a-2)-(d-2) and 18(e-2)-(h-2) show the relationship between wave height h_w and BER (fixed wave frequency f_w) and that between wave frequency f_w and BER (fixed wave height hw), respectively. From these figures, we found that the BERs of PSK, NRZ-OOK, and OFDM are less than 10^{-4} when there is no wave. On the other hand, the BER of NRZ-OOK increases when there is a surface wave, while the BER of PSK or OFDM remains less than 10^{-4}. This is because the amplitude of the received NRZ-OOK signal changes dynamically by a surface wave within the signal block, making it difficult for the Rx to determine an optimal threshold, as was the case in the preliminary experiments. In contrast, the effect of low-frequency ambient light scattered by a surface wave can be avoided in PSK or OFDM, as described in Section III-A.

As shown in Figs. 18(a-2)-(d-2), the BERs of PSK and OFDM also increase in proportion to the wave height h_w. This is because the intensity of the ambient light increases in proportion to h_w [Fig. 17(f-1)-(i-1)], causing pixel saturation. Also, the BER of OFDM due to pixel saturation is larger than that of PSK, since the high PAPR modulation technique is more likely to result in pixel saturation, as described in Section III-B.

Consequently, we reveal that the VLC system using PSK or OFDM outperformed that using NRZ-OOK in an underwater channel with low-frequency ambient light, and that PSK outperformed OFDM in the underwater channel with dynamically changing ambient light intensity. Therefore, an underwater VLC system using PSK could be a viable alternative by utilizing the image sensor as the Rx in environments with high ambient light conditions.

VII. CONCLUSION

In this study we proposed an underwater VLC system using a rolling-shutter sensor and revealed the optimal signal modulation technique for underwater environments with high ambient light conditions. Three modulation techniques [(a) PSK (proposed), (b) NRZ-OOK (existing), and (c) OFDM (existing)] were compared and evaluated through simulations and experiments that considered two characteristics of the channel and sensor (A. interference of ambient light, B. pixel saturation). The simulation and experimental results

suggested that the VLC system using PSK or OFDM is more resilient than that using NRZ-OOK in an underwater channel with low-frequency ambient light, and that the VLC system using PSK or NRZ-OOK is more tolerant than that using OFDM in underwater environments with high ambient light, resulting in pixel saturation. Therefore, PSK was found to be the optimal modulation technique for the VLC system using a rolling-shutter sensor in underwater environments with high ambient light conditions. The proposed system using a rolling-shutter sensor and PSK can contribute to the establishment of a short-range and reliable underwater wireless communication link.

On the other hand, actual underwater environments are much more complex, with many factors that affect underwater VLC. Hence, we are planning to conduct experiments in actual environments in our future works. In this paper we do not consider the use of theoretical equations, since a precise model of a complex underwater communication channel is necessary. However, the use of theoretical equations has an advantage in that the performance of a communication system can be continuously evaluated by changing the parameters. Hence, in the future we also plan to evaluate the performance of communication systems using theoretical equations by collecting the information necessary to model complex underwater channels in real environments.

APPENDIX

A. MODULATION AND DEMODULATION TECHNIQUES

1) NRZ-OOK

Modulation: The NRZ-OOK-modulated payload signal $p_l^{\text{NRZ-OOK}}(t')$ can be expressed as

$$p_l^{\text{NRZ-OOK}}(t') = \begin{cases} a + a_{\text{off}} & (b_{l,n} = 1) \\ -a + a_{\text{off}} & (b_{l,n} = 0) \end{cases} \left[\frac{n}{N} T_{\text{d}} \le t' < \frac{n+1}{N} T_{\text{d}} \right], \quad (3)$$

where $a > 0$ and a_{off} are the signal amplitude and the DC offset to make $p_l^{\text{NRZ-OOK}}(t')$ positive, respectively.

Demodulation: The received signal $\tilde{p}_l^{\text{NRZ-OOK}}[k']$ can be expressed by (2) and (3) as

$$\tilde{p}_l^{\text{NRZ-OOK}}[k'] = p_l^{\text{NRZ-OOK}}\left[\frac{T_{\text{f}}}{K} k' \right] + a_{\text{off}} + n\left[\frac{T_{\text{f}}}{K} k' \right].$$

Then, the Rx demodulates the binary data block $\tilde{b}_{l,n}$ from the received signal and the threshold value $v_{threshold}$.

$$\tilde{b}_{l,n} = \begin{cases} 1 & (\tilde{p}_l^{\text{NRZ-OOK}}[k'] \ge v_{threshold}) \\ 0 & (\tilde{p}_l^{\text{NRZ-OOK}}[k'] < v_{threshold}) \end{cases} \left[\frac{T_{\text{d}} n}{T_{\text{f}} N} K \le k' < \frac{T_{\text{d}}(n+1)}{T_{\text{f}} N} K \right].$$

2) PSK

Modulation: The Tx converts the binary data $b_{l,n}$ to the symbol data $d_{l,n}$, defined as

$$d_{l,n} = \begin{cases} 1 & (b_{l,n} = 1) \\ -1 & (b_{l,n} = 0). \end{cases} \quad (4)$$

The Tx performs PSK modulation by multiplying the symbol data $d_{l,n}$ and carrier signals of the frequency of f_{c}. The PSK-modulated payload signal $p_l^{\text{PSK}}(t')$ can be expressed as

$$p_l^{\text{PSK}}(t') = \frac{a}{\sqrt{2}} \Re\left[d_{l,n} e^{j2\pi f_{\text{c}} t'} \right] + a_{\text{off}} \left[\frac{n}{N} T_{\text{d}} \le t' < \frac{n+1}{N} T_{\text{d}} \right]. \quad (5)$$

Note that $a/\sqrt{2}$ is a factor to make each signal power the same.

Demodulation: The received signal $\tilde{p}_l^{\text{PSK}}[k']$ can be expressed by (2) and (5) as

$$\tilde{p}_l^{\text{PSK}}[k'] = \Re\left[d_{l,n} e^{j2\pi f_{\text{c}} \frac{T_{\text{f}}}{K} k'} \right] + a_{\text{off}} + n\left[\frac{T_{\text{f}}}{K} k' \right] \left[\frac{T_{\text{d}} n}{T_{\text{f}} N} K \le k' < \frac{T_{\text{d}}(n+1)}{T_{\text{f}} N} K \right]. \ [0 \le t' < T_{\text{d}}] \quad (6)$$

The receiver applies a high-pass filter to (6) to remove a_{off} and $n\left[T_{\text{f}} k'/K\right]$. The filtered payload signal can be expressed as

$$\tilde{p}_{\text{Hl}}^{\text{PSK}}[k'] = \Re\left[d_{l,n} e^{j2\pi f_{\text{c}} \frac{T_{\text{f}}}{K} k'} \right]$$

Then, the Rx multiplies the filtered signal by the carrier, as shown in (7) and (8),

$$\begin{aligned} &\tilde{p}_{\text{Hl}}^{\text{PSK}}[k'] \cos\left(2\pi f_{\text{c}} \frac{T_{\text{f}}}{K} k'\right) \\ &= \tilde{a}_{l,n} \cos^2\left(2\pi f_{\text{c}} \frac{T_{\text{f}}}{K} k'\right) \\ &\quad - \tilde{b}_{l,n} \sin\left(2\pi f_{\text{c}} \frac{T_{\text{f}}}{K} k'\right)\left(\cos 2\pi f_{\text{c}} \frac{T_{\text{f}}}{K} k'\right) \\ &= \frac{\tilde{a}_{l,n}}{2} + \frac{\tilde{a}_{l,n}}{2} \cos\left(4\pi f_{\text{c}} \frac{T_{\text{f}}}{K} k'\right) \\ &\quad - \frac{\tilde{b}_{l,n}}{2} \sin\left(4\pi f_{\text{c}} \frac{T_{\text{f}}}{K} k'\right), \end{aligned} \quad (7)$$

$$\begin{aligned} &\tilde{p}_{\text{Hl}}^{\text{PSK}}[k']\left\{-\sin\left(2\pi f_{\text{c}} \frac{T_{\text{f}}}{K} k'\right)\right\} \\ &= -\tilde{a}_{l,n} \cos\left(2\pi f_{\text{c}} \frac{T_{\text{f}}}{K} k'\right)\left(\sin 2\pi f_{\text{c}} \frac{T_{\text{f}}}{K} k'\right) \\ &\quad + \tilde{b}_{l,n} \sin^2\left(2\pi f_{\text{c}} \frac{T_{\text{f}}}{K} k'\right) \\ &= \frac{\tilde{b}_{l,n}}{2} + \frac{\tilde{b}_{l,n}}{2} \cos\left(4\pi f_{\text{c}} \frac{T_{\text{f}}}{K} k'\right) \\ &\quad - \frac{\tilde{a}_{l,n}}{2} \sin\left(4\pi f_{\text{c}} \frac{T_{\text{f}}}{K} k'\right), \end{aligned} \quad (8)$$

where

$$\tilde{d}_{l,n} = \tilde{a}_{l,n} + j\tilde{b}_{l,n}.$$

Finally, the Rx gets $\tilde{a}_{l,n}$ and $\tilde{b}_{l,n}$ by applying a low-pass filter to (7) and (8), and obtains the binary data $\tilde{b}_{l,n}$ from the data symbols $\tilde{d}_{l,n} = \tilde{a}_{l,n} + j\tilde{b}_{l,n}$.

3) OFDM

Modulation: The Tx calculates IFFT (inverse fast fourier transform) of each set of symbols d_{n} (4). The baseband-OFDM (BB-OFDM) modulated payload signal $p_l^{\mathrm{OFDM}}(t')$ can be expressed as

$$p_l^{\text{BB-OFDM}}(t') = \sqrt{\frac{2}{N}} a \Re\left[\sum_{n=0}^{N-1} d_{l,n} e^{j2\pi n f_0 t'}\right] + a_{\mathrm{off}}, \quad (9)$$

where

$$f_0 = \frac{1}{T_{\mathrm{d}}}.$$

Note that $\sqrt{2/N}a$ is a factor to make each signal power the same. Then, the Tx performs OFDM modulation by multiplying the BB-OFDM signal $p_l^{\text{BB-OFDM}}(t')$ and carrier signals of the frequency of f_{c}. The OFDM-modulated payload signal $p_l^{\mathrm{OFDM}}(t')$ can be expressed as

$$p_l^{\mathrm{OFDM}}(t') = \sqrt{\frac{2}{N}} a \Re\left[\sum_{n=0}^{N-1} d_{l,n} e^{j2\pi (f_{\mathrm{c}} + n f_0) t'}\right] + a_{\mathrm{off}}. \quad (10)$$

Demodulation: The received signal $\tilde{p}_l^{\mathrm{OFDM}}[k']$ can be expressed by (2) and (10) as

$$\tilde{p}_l^{\mathrm{OFDM}}[k'] = \Re\left[\sum_{n=0}^{N-1} \tilde{d}_{l,n} e^{j2\pi (f_{\mathrm{c}} + n f_0) \frac{T_{\mathrm{f}}}{K} k'}\right] + a_{\mathrm{off}} + n\left[\frac{T_{\mathrm{f}}}{K} k'\right]. \quad (11)$$

The receiver applies a high-pass filter to (11) to remove a_{off} and $n\left[T_{\mathrm{f}} k'/K\right]$. The filtered payload signal can be expressed as

$$\tilde{p}_l^{\mathrm{OFDM}}[k'] = \Re\left[\sum_{n=0}^{N-1} \tilde{d}_{l,n} e^{j2\pi (f_{\mathrm{c}} + n f_0) \frac{T_{\mathrm{f}}}{K} k'}\right]. \quad (12)$$

Then, the Rx multiplies the filtered signal by the carrier, as shown in (13) and (14),

$$\tilde{p}_{lI}[k'] = \sum_{n=0}^{N-1} \{\tilde{a}_{l,n} \cos(2\pi n f_0 t') - \tilde{b}_{l,n} \sin(2\pi n f_0 t')\}, \quad (13)$$

$$\tilde{p}_{lQ}[k'] = \sum_{n=0}^{N-1} \{-\tilde{a}_{l,n} \sin(2\pi n f_0 t') + \tilde{b}_{l,n} \cos(2\pi n f_0 t')\}. \quad (14)$$

From (13) and (14), the baseband payload signal $\tilde{u}_l[k']$ can be expressed as

$$u_l[k'] = \tilde{p}_{lI}[k'] + j\tilde{p}_{lQ}[k'] = \sum_{n=0}^{N-1} \tilde{d}_{l,n} e^{j2\pi n f_0 \frac{T_{\mathrm{f}}}{K} k'}.$$

When $\tilde{u}_l[k']$ is sampled at N points, $\tilde{u}_l[k']$ can be expressed as

$$\tilde{u}_l\left[\frac{m}{N f_0}\right] = e^{\frac{T_{\mathrm{f}}}{K}} \sum_{n=0}^{N-1} \tilde{d}_{l,n} e^{j\frac{2\pi nm}{N}}, \quad [m = 0, 1, \ldots, N-1]. \quad (15)$$

Then, the data symbols $\tilde{d}_{l,n}$ can be obtained by performing of (15), as shown in (16).

$$\tilde{d}_{l,n} = \frac{e^{\frac{T_{\mathrm{f}}}{K}}}{N} \sum_{n=0}^{N-1} u_l\left[\frac{m}{N f_0}\right] e^{-j\frac{2\pi nm}{N}}. \quad (16)$$

Finally, the Rx gets $\tilde{a}_{l,n}$ and $\tilde{b}_{l,n}$ and obtains the binary data $\tilde{b}_{l,n}$ from the data symbols $\tilde{d}_{l,n} = \tilde{a}_{l,n} + j\tilde{b}_{l,n}$

ACKNOWLEDGMENT

The authors would like to thank Dr. T. Sekiguchi and H. Iijima of the Center for Research in Isotopes and Environmental Dynamics, University of Tsukuba, for providing the experimental environment.

REFERENCES

[1] O. Gupta, N. Goyal, D. Anand, S. Kadry, Y. Nam, and A. Singh, "Underwater networked wireless sensor data collection for computational intelligence techniques: Issues, challenges, and approaches," *IEEE Access*, vol. 8, pp. 122959–122974, 2020, doi: 10.1109/ACCESS.2020.3007502.

[2] M. Stojanovic, "Recent advances in high-speed underwater acoustic communications," *IEEE J. Ocean. Eng.*, vol. 21, no. 2, pp. 125–136, Apr. 1996.

[3] M. Chitre, S. Shahabudeen, L. Freitag, and M. Stojanovic, "Recent advances in underwater acoustic communications & networking," in *Proc. IEEE OCEANS*, Quebec City, QC, Canada, Oct. 2009, pp. 1–10.

[4] I. F. Akyildiz, P. Wang, and Z. Sun, "Realizing underwater communication through magnetic induction," *IEEE Commun. Mag.*, vol. 53, no. 11, pp. 42–48, Nov. 2015.

[5] H. Kaushal and G. Kaddoum, "Underwater optical wireless communication," *IEEE Access*, vol. 4, pp. 1518–1547, 2016.

[6] H. M. Oubei, C. Shen, A. Kammoun, E. Zedini, K.-H. Park, X. Sun, G. Liu, C. H. Kang, T. K. Ng, and M.-S. Alouini, "Light based underwater wireless communications," *Jpn. Soc. Appl. Phys.*, vol. 57, no. 8S2, Jul. 2018, Art. no. 08PA06.

[7] S. Tang, Y. Dong, and X. Zhang, "Impulse response modeling for underwater wireless optical communication links," *IEEE Trans. Commun.*, vol. 62, no. 1, pp. 226–234, Jan. 2014, doi: 10.1109/TCOMM.2013.120713.130199.

[8] T. Nguyen, A. Islam, M. T. Hossan, and Y. M. Jang, "Current status and performance analysis of optical camera communication technologies for 5G networks," *IEEE Access*, vol. 5, pp. 4574–4594, 2017.

[9] R. L. P. de Lima, F. C. Boogaard, and R. E. de Graaf-van Dinther, "Innovative water quality and ecology monitoring using underwater unmanned vehicles: Field applications, challenges and feedback from water managers," *MDPI Water*, vol. 12, no. 4, p. 1196, Apr. 2020.

[10] H. M. Oubei, C. Li, K. H. Park, T. K. Ng, M. S. Alouini, and B. S. Ooi, "2.3 Gbit/s underwater wireless optical communications using directly modulated 520 nm laser diode," *Opt. Exp.*, vol. 23, no. 16, pp. 20743–20748, 2015.

[11] K. Nakamura, I. Mizukoshi, and M. Hanawa, "Optical wireless transmission of 405 nm, 1.45 Gbit/s optical IM/DD-OFDM signals through a 4.8 m underwater channel," *Opt. Exp.*, vol. 23, no. 2, pp. 1558–1566, 2015.

[12] H. M. Oubeietal, "4.8 Gbit/s 16-QAM-OFDM transmission based on compact 450-nm laser for underwater wireless optical communication," *Opt. Exp.*, vol. 23, no. 18, pp. 23302–23309, 2015.

[13] J. Baghdady, K. Miller, K. Morgan, M. Byrd, S. Osler, R. Ragusa, W. Li, B. M. Cochenour, and E. G. Johnson, "Multi-gigabit/s underwater optical communication link using orbital angular momentum multiplexing," *Opt. Exp.*, vol. 24, no. 9, p. 9794, 2016.

[14] C. Shen, Y. Guo, H. M. Oubei, T. K. Ng, G. Liu, K.-H. Park, K.-T. Ho, M.-S. Alouini, and B. S. Ooi, "20-meter underwater wireless optical communication link with 15 Gbps data rate," *Opt. Exp.*, vol. 24, no. 22, p. 25502, 2016.
[15] Y.-F. Huang, C.-T. Tsai, Y.-C. Chi, D.-H. Huang, and G.-R. Lin, "Filtered multicarrier OFDM encoding on blue laser diode for 14.8-Gbps seawater transmission," *J. Lightw. Technol.*, vol. 36, no. 9, pp. 1739–1745, May 1, 2018.
[16] X. Liu, S. Yi, X. Zhou, Z. Fang, Z. Qiu, L. Hu, C. Cong, L. Zheng, R. Liu, and P. Tian, "34.5 m underwater optical wireless communication with 2.70 Gbps data rate based on a green laser diode with NRZ-OOK modulation," *Opt. Exp.*, vol. 25, no. 22, pp. 27937–27947, Oct. 2017.
[17] Y. Chen, M. Kong, T. Ali, J. Wang, R. Sarwar, J. Han, C. Guo, B. Sun, N. Deng, and J. Xu, "26 m/5.5 Gbps air-water optical wireless communication based on an OFDM-modulated 520-nm laser diode," *Opt. Exp.*, vol. 25, no. 13, pp. 14760–14765, Jun. 2017.
[18] S. Nishimoto, T. Yamazato, H. Okada, T. Fujii, T. Yendo, and S. Arai, "High-speed transmission of overlay coding for road-to-vehicle visible light communication using LED array and high-speed camera," in *Proc. IEEE Globecom Workshops*, Anaheim, CA, USA, Dec. 2012, pp. 1234–1238.
[19] C.-W. Chow, C.-Y. Chen, and S.-H. Chen, "Enhancement of signal performance in LED visible light communications using mobile phone camera," *IEEE Photon. J.*, vol. 7, no. 5, pp. 1–7, Oct. 2015.
[20] M. Akram, R. Godaliyadda, and P. Ekanayake, "Design and analysis of an optical camera communication system for underwater applications," *IET Optoelectron.*, vol. 14, no. 1, pp. 10–21, Feb. 2020, doi: 10.1049/iet-opt.2018.5157.
[21] Z. Zhou, S. Wen, Y. Li, W. Xu, Z. Chen, and W. Guan, "Performance enhancement scheme for RSE-based underwater optical camera communication using de-bubble algorithm and binary fringe correction," *Electronics*, vol. 10, no. 8, p. 950, Apr. 2021.
[22] Y. Liu, H.-Y. Chen, K. Liang, C.-W. Hsu, C.-W. Chow, and C.-H. Yeh, "Visible light communication using receivers of camera image sensor and solar cell," *IEEE Photon. J.*, vol. 8, no. 1, pp. 1–7, Feb. 2016.
[23] K. Liang, C.-W. Chow, Y. Liu, and C.-H. Yeh, "Thresholding schemes for visible light communications with CMOS camera using entropy-based algorithms," *Opt. Exp.*, vol. 24, no. 22, pp. 25641–25646, 2016.
[24] D. Wulich, "Definition of efficient PAPR in OFDM," *IEEE Commun. Lett.*, vol. 9, no. 9, pp. 832–834, Sep. 2005.
[25] A. Toffoli and E. M. Bitner-Gregersen, "Types of ocean surface waves, wave classification," in *Encyclopedia of Maritime and Offshore Engineering*, J. Carlton, P. Jukes, and Y. S. Choo, Eds. Hoboken, NJ, USA: Wiley, 2017, pp. 1–8, doi: 10.1002/9781118476406.emoe077.

RITSUKI HAMAGAMI (Graduate Student Member, IEEE) was born in Tokyo, Japan, in 1998. He received the B.Eng. degree from the University of Tsukuba, Tsukuba, Japan, in 2020, where he is currently pursuing the degree in intelligent and mechanical interaction systems. His research interest includes underwater visible light communication. He is a Student Member of the Institute of Electronics, Information and Communication Engineers (IEICE) of Japan.

TADASHI EBIHARA (Member, IEEE) was born in Tokyo, Japan, in 1986. He received the Ph.D. degree from the University of Tsukuba, Tsukuba, Japan, in 2010. From September 2013 to December 2013, he was a Visiting Professor with the Delft University of Technology, The Netherlands. He is currently with the Graduate School of Systems and Information Engineering, University of Tsukuba. He is also an Associate Professor with the Faculty of Engineering, Information and Systems, University of Tsukuba. His research interests include mobile communications and their applications to underwater acoustic communication systems. He received a Research Fellowship for Young Scientists (DC1) from the Japan Society for the Promotion of Science (JSPS), in 2009 and 2010. He also received the 2017 IEEE Oceanic Engineering Society Japan Chapter Young Researcher Award.

NAOTO WAKATSUKI received the B.Eng., M.Eng., and D.Eng. degrees from the University of Tsukuba, Tsukuba, Japan, in 1993, 1995, and 2004, respectively. He was with Okayama University, from 1995 to 2001, and Akita Prefectural University, from 2001 to 2006. He is currently with the Graduate School of Systems and Information Engineering, University of Tsukuba. He is also an Associate Professor with the Faculty of Engineering, Information and Systems, University of Tsukuba. His research interests include acoustic instrumentation, simulation-based visualization, vibration sensors and actuators, acoustical engineering, musical acoustics, and inverse problems. His affiliated academic societies include the Acoustical Society of Japan, the Acoustical Society of America, the Society of Agricultural Structures, and the Japan Society for Simulation Technology.

KOICHI MIZUTANI graduated from the National Defense Academy, in 1979. He received the Ph.D. degree in engineering from Kyoto University, in 1990. He was a Researcher with the Department of Electrical Engineering, National Defense Academy, from 1984 to 1988, and the Department of Research, Communication and Intelligence School, Japanese Ground Self Defense Force (JGSDF), from 1988 to 1990. He was the Deputy Director of the Secretariat of the Director General of the National Defense Agency, from 1991 to 1992. He retired from JGSDF at the rank of Major. He joined the Faculty of the Institute of Applied Physics, University of Tsukuba, Tsukuba, Japan, as an Assistant Professor, in 1992, an Associate Professor, in 1998, and a Full Professor, in 2004, where he is currently a Researcher (full-time) with the Faculty of Engineering, Information and Systems. He was given the title Emeritus Professor with the University of Tsukuba, in 2021. He has been engaged in research on ultrasonic electronics, medical electronics, welfare technologies, complementation of human sensory functions, robot sensing, communication systems in sensing grids, environment monitoring, applied optics, applied acoustics, musical acoustics, food and agricultural engineering, and health monitoring engineering of livestock. He is a member of the Society of Agricultural Structures, Japan (SASJ), the Marine Acoustics Society of Japan (MASJ), the Japan Society of Civil Engineering (JSCE), and the Japan Society of Applied Physics (JSAP).